

# Fluorescence Interference-Based Polarized Structured Illumination Microscopy for High Axial Accuracy Morphology Imaging of Dipole Orientations

Yile Sun,<sup>▼</sup> Hongfei Zhu,<sup>▼</sup> Xinxun Yang, Enxing He, Hanmeng Wu, Lu Yin, Weiyun Sun, Xin Luo, Yubing Han, Xiang Hao, Renjie Zhou, Cuifang Kuang,\* and Xu Liu



Cite This: *ACS Photonics* 2025, 12, 419–428



Read Online

ACCESS |

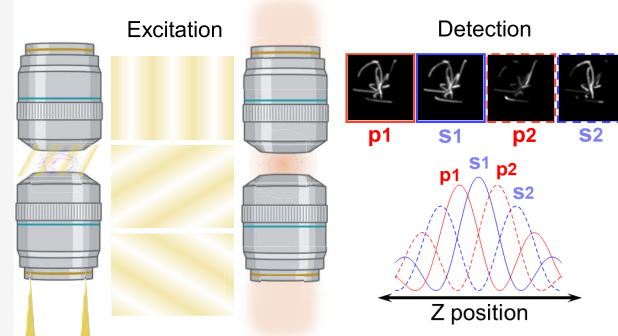
Metrics & More

Article Recommendations

Supporting Information

**ABSTRACT:** The dipole orientation of fluorescent molecules reveals the structural organization at the subcellular level, and imaging its distribution is important for fundamental cell biology studies. Using conventional fluorescence microscopy, the orientation of fluorescent dipoles can be obtained by demodulating the polarization states through excitation or emission processes. The recent introduction of structured illumination microscopy (SIM) has improved the axial and lateral resolution to around 300 and 100 nm, respectively. However, the axial resolution is still very limited, which hinders the capabilities to offer more precise measurements of polarization information. Here, we report Fluorescence Interference based polarized structured illumination microscopy (FI-pSIM), which provides a sub-30 nm axial reconstruction accuracy and maintains the same lateral resolution comparable to SIM by only 9 raw images. By synergizing the fluorescence interference via the 4Pi configuration and the polarization demodulation of structured illumination, FI-pSIM enables three-dimensional morphological imaging of ensemble dipole orientations in subcellular structures with ~ sub-30 nm accuracy of axial reconstruction. The high efficacy and four-dimensional (4D) imaging modality of FI-pSIM are demonstrated by mapping the distribution and orientation of fluorescent dipoles in biological microfilaments. By elucidating the dipole orientations, we envision FI-pSIM may open up new avenues for demystifying the 4D organizations of subcellular structures.

**KEYWORDS:** polarization microscopy, 4Pi microscopy, structured illumination microscopy



## INTRODUCTION

Fluorescence microscopy has become an essential tool for studying cells and subcellular structures.<sup>1–5</sup> The advent of super-resolution fluorescence microscopy has allowed for the observation of finer details in these structures by offering spatial resolution at sub-10 nm,<sup>6–10</sup> and more recently at the Angstrom level.<sup>11,12</sup> Meanwhile, the development of polarization microscopy (PM) has provided cell biologists with new structural information from the fluorescent molecules that act as dipole emitters.<sup>13–16</sup> When the connections between fluorescent molecules and subcellular structures are relatively rigid,<sup>17</sup> the wobble of the fluorescent dipoles can be substantially constrained, resulting in high polarization dependence of fluorescence signals in both excitation and emission processes.<sup>13</sup> This effect is more prominent when employing high numerical aperture (NA) objective lenses.

Elucidating the dipole orientations in subcellular structures requires high spatial resolution, which has promoted great efforts in recent years in implementing super-resolution imaging strategies in polarization microscopy. The developed techniques

can be divided into two primary categories: single-molecule orientation and localization microscopy (SMOLM)<sup>18–27</sup> and polarized structured illumination microscopy (pSIM).<sup>28</sup> SMOLM captures the three-dimensional (3D) orientation of dipoles by utilizing the shape and intensity of the point spread function (PSF), achieving a high spatial resolution to sub-50 nm. However, as SMOLM is based on single-molecule localization microscopy, it inevitably exhibits severe phototoxicity and Photobleaching.<sup>29</sup> By introducing polarization demodulation<sup>30,31</sup> in SIM,<sup>3,32</sup> pSIM can double the lateral resolution of conventional PM.<sup>28</sup> With axial scanning and 3D-SIM reconstruction algorithms,<sup>33</sup> pSIM has been recently extended to 3D imaging of dipole orientations.<sup>34,35</sup> Most current pSIM

Received: September 19, 2024

Revised: December 19, 2024

Accepted: December 19, 2024

Published: December 30, 2024



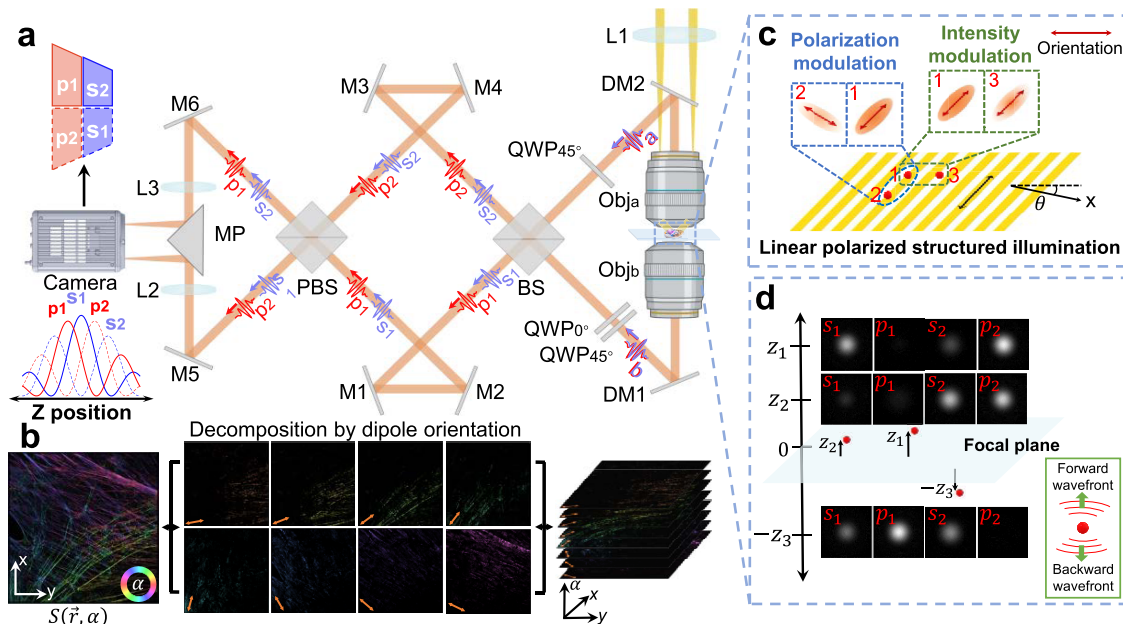


**Figure 1.** Working principles of FI-pSIM. (a) Schematic setup of the optical system. (b) Illustration of the polarization demodulation principle for dipole orientation reconstruction. (c) Illustration of polarization and intensity modulation. Dipole 1 and 2 are with the same illumination intensity but different orientations, while dipole 1 and 3 are with the same orientation but different illumination intensities. (d) Illustration of fluorescence interference at different depths. The polarization information is derived from linearly polarized structured illumination, and the high axial reconstruction accuracy is obtained from fluorescence interference. L: lens; M: mirror; PBS: polarization beam splitter; BS: beam splitter; QWP: quarter wave plate; DM: dichroic mirror; Obj: objective lens; MP: reflective prism.

methods modulate the projection of each 3D dipole onto the transverse plane,<sup>13</sup> thus ignoring the longitudinal orientation (polar angle).<sup>36</sup> Despite missing comprehensive 3D dipole information, these systems can obtain azimuthal information of dipoles in the transverse plane, which reflects the ensemble orientations. Meanwhile, the low phototoxicity and fast data acquisition speed capabilities render pSIM well-suited for live-cell imaging.<sup>37,38</sup> However, the performance of pSIM in the axial direction remains constrained to around 300 nm, making it challenging to decipher finer structural organization.<sup>34,35</sup> Despite the emergence of several SIM techniques in recent years that can achieve better than 300 nm axial resolution—such as those utilizing 4Pi configuration,<sup>39</sup> total internal reflection fluorescence microscopy (TIRF),<sup>40</sup> the introduction of additional excitation beams,<sup>41,42</sup> and methods combining deep learning,<sup>42,43</sup> which can achieve axial resolutions of 160 nm or even higher—these approaches are difficult to apply to polarization microscopy, and axial resolution remains limited to above 100 nm.

Here, we report a new imaging modality, fluorescence interference-based polarized illumination microscopy (FI-pSIM) for mapping the organizations of subcellular structures with high axial accuracy, thus achieving super-resolution four-dimensional (4D) imaging. Via polarization demodulation of structured illumination and fluorescence interference<sup>44,45</sup> of 4Pi configuration, FI-pSIM can reconstruct the ensemble dipole orientations and axial distribution of the sample with sub-30 nm axial accuracy, eliminating the need for axial scanning that is cumbersome in many bioimaging scenarios. It also maintains a lateral resolution of around 100 nm. Our extensive imaging experimental results on fixed cells have shown that FI-pSIM is a promising high-efficiency 4D imaging tool for simultaneous retrieval of both structural and polarization information within subcellular structures.

## METHODS

FI-pSIM is based on three core techniques: (i) axial reconstruction by fluorescence interference with sub-30 nm axial accuracy; (ii) dipole orientation reconstruction by polarization demodulation with around 100 nm lateral resolution; and (iii) synergizing both axial reconstruction and dipole orientation reconstruction for 4D imaging of subcellular structures. Their working principles are illustrated in Sections 2.1–2.3 in the following.

**Axial Reconstruction by Fluorescence Interference.** Following the original work of 4Pi single-molecule switching fluorescence microscopy (4Pi-SMS),<sup>46</sup> we have implemented a high axial reconstruction accuracy strategy based on a 4Pi configuration. As illustrated in Figure 1a, the 4Pi cavity comprises two opposing objective lenses ( $\text{Obj}_a$  and  $\text{Obj}_b$ ) that collect backward and forward fluorescence signals in the upper and lower detection paths, respectively. When the optical path difference between the two paths is tuned to be within the coherence length of the fluorescence emission (usually on the micrometer level<sup>45</sup>), fluorescence interference occurs at the beam splitter (BS) in Figure 1a. The intensity of fluorescence interference is sensitive to the sample axial variation, which is encoded into the phases of the fluorescence.<sup>39,47–49</sup> To decode the axial information, a four-step fluorescence phase shifting technique is implemented by the combination of quarter wave plates (QWP), the BS and a polarized beam splitter (PBS) in the detection path. Theoretically, the fluorescence after interference is divided into four channels with  $\frac{\pi}{2}$  intervals (Figure 1d), and the axial information can be calculated through the four channels. The fluorescence signals of each channel are expressed as

$$\begin{cases} s_1 = 1 + m \cos(\varphi + \Delta\varphi_s) \\ s_2 = 1 - m \cos(\varphi + \Delta\varphi_s) \\ p_1 = 1 + m \cos(\varphi + \Delta\varphi_p) \\ p_2 = 1 - m \cos(\varphi + \Delta\varphi_p) \end{cases} \quad (1)$$

where  $s$  and  $p$  represent the polarization component of fluorescence signals divided by the BS and PBS in Figure 1a;  $\varphi=2k_0z$  is the phase measured from the focal plane, and  $k_0 = 2\pi/\lambda$ ;  $\lambda$  is the emission wavelength in the sample medium;  $m$  is a constant obtained from adding up amplitudes of fluorescence during interference;  $\Delta\varphi_s$  and  $\Delta\varphi_p$  are the phase differences of  $s$  and  $p$  components between fluorescence signals collected by upper and lower objective lenses, respectively, which need to be calibrated carefully by adjusting the orientations of fast axes of QWPs. In practice, the specific values of  $\Delta\varphi_s$  and  $\Delta\varphi_p$  are measured in advance through 100 nm fluorescent beads (Note S6 in the Supporting Information). The actual average phase shift  $\Delta\varphi = \Delta\varphi_p - \Delta\varphi_s$  generated by QWP0° is around 75° (0.42π). Therefore, the equivalent values of  $\Delta\varphi_p$  and  $\Delta\varphi_s$  in Figure 1a are 75° and 0. By solving eq 1,  $\varphi$  and the axial position can be obtained. It should be noted that the value of  $\varphi$  will be located between  $[-\pi, +\pi]$  (corresponding to an axial range of half wavelength) due to the periodicity of cosine functions. The original phases can be obtained using phase unwrapping algorithms that add appropriate multiples of  $2\pi$  to each phase input. Consequently, the phase change will be smoother without any abrupt transitions of  $2\pi$ , and the axial detection range can thus be extended to multiple wavelengths ( $z=\varphi/2k_0$ ).

Different from localizing individual blinking fluorophores in 4Pi-SMS, in our wide-field implementation, eq 1 is utilized under ensemble conditions. For each channel, the average intensity of a region of interest (ROI) is chosen as the effective intensity of the central pixel of the ROI, while the range of the ROI is determined from the density of the sample in the field of view. Note that ROI is smaller compared to the diffraction spot size, and we assume the slowly varying continuity condition in biological samples as what has been done previously.<sup>40,50</sup> The relation of effective intensity of the central pixel within the ROI in each channel is approximately consistent with the intensity under single-molecule conditions. From our previous research,<sup>50</sup> the achievable ensemble axial accuracy is sub-30 nm, which is slightly worse than the localization precision of 4Pi-SMS<sup>46</sup> and 4Pi stochastic optical reconstruction microscopy (4Pi-STORM).<sup>51</sup> This is due to the existence of surrounding emitters, which average the fluorescence signals within the ROI. However, the ensemble axial reconstruction in FI-pSIM uses the average depth of a group of fluorophores in each ROI, which improves the robustness to noise.

To achieve around 100 nm lateral resolution, we applied the 2D-SIM reconstructed image as a spatial mask to implement the ensemble axial reconstruction. Although 3D-SIM can provide a better optical sectioning effect, we choose the 2D-SIM modality with two interference beams to avoid the insensitive response of dipoles to excitation beams issues due to the use of a circularly polarized excitation beam (the middle beam) in most 3D-SIM systems.<sup>52</sup> Recently, Li et al.<sup>34</sup> reported a new system that can synchronously adjust the polarization and intensity of the middle beam with a digital micromirror device (DMD) and an attenuation filter. This method can settle the circular-polarization issue of the middle excitation beam as mentioned and

will be an important reference for optimizing the FI-pSIM system in the future. Although the optical sectioning effect is weakened, FI-pSIM can still obtain the axial distribution of continuously distributed samples which is beyond half wavelength depth through the phase unwrapping method,<sup>6,7,46</sup> with extending the axial detection range appropriately.

### Dipole Orientation Reconstruction by Polarization Modulation.

In pSIM, the fluorescence emission intensity is modulated by two factors: (i) the illumination intensity of the interference pattern  $I_{\theta,\phi}(\vec{r})$ , where  $\theta$  and  $\phi$  denote the orientation and global phase of the sinusoidal fringes, respectively; and (ii) the response of dipoles to linearly polarized illumination  $P_\theta(\alpha)$ , where  $\alpha$  is the azimuthal angle of dipoles. The corresponding fluorescence intensity  $D_{\theta,\phi}(\vec{r})$  at position  $\vec{r} = (x, y)$  can be expressed as

$$D_{\theta,\phi}(\vec{r}) = \int_a d\vec{a} [S(\vec{r}, \alpha) \cdot I_{\theta,\phi}(\vec{r}) \cdot P_\theta(\alpha)] \otimes_{\vec{r}} h(\vec{r}, \alpha) \quad (2)$$

where  $S(\vec{r}, \alpha)$  represents the density distribution of fluorophores at each azimuthal dipole angle  $\alpha$  (Figure 1b,c), and  $h(\vec{r}, \alpha)$  is the dipole point spread function with dipole azimuthal angle  $\alpha$ . More detailed derivations of  $I_{\theta,\phi}(\vec{r})$  and  $P_\theta(\alpha)$  are included in Note S1 of the Supporting Information. The mathematical model of  $h(\vec{r}, \alpha)$  can be found in Note S2 of the Supporting Information. Since the polarization of the illumination is within the transverse sample plane, the measured dipole orientation is reduced to a 2D distribution,<sup>36,53</sup> that is, the dipole azimuth angle. Compared with uniform linearly polarized illumination, polarized spatial structured illumination will not encode more angular information into the detected data but is used for lateral resolution improvement. We can use Fourier series  $e^{ima}$  ( $\alpha \in [0, 2\pi]$ ,  $m \in \mathbb{N}$ ) to decompose both  $S(\vec{r}, \alpha)$  and  $h(\vec{r}, \alpha)$

$$S(\vec{r}, \alpha) = \sum_{n=-\infty}^{\infty} a_{2n}(\vec{r}) e^{i2n\alpha} \quad (3a)$$

$$h(\vec{r}, \alpha) = \sum_{m=-2}^{m=2} b_m(\vec{r}) \cdot e^{ima} \quad (3b)$$

And there exists an angular band limit for the imaging system; we only get the information on specific orders of  $a_{2n}(\vec{r})$

$$\begin{aligned} B_{\theta,1}(\vec{k}) = & 2\pi \left[ \left( \frac{e^{-i2\theta}}{2} \tilde{b}_2(\vec{k}) \right) \tilde{a}_{-4}(\vec{k}) \right. \\ & + \left( \tilde{b}_2(\vec{k}) + \frac{e^{-i2\theta}}{2} \tilde{b}_0(\vec{k}) \right) \tilde{a}_{-2}(\vec{k}) \\ & + \left( \frac{e^{i2\theta}}{2} \tilde{b}_2(\vec{k}) + \tilde{b}_0(\vec{k}) + \frac{e^{-i2\theta}}{2} \tilde{b}_{-2}(\vec{k}) \right) \tilde{a}_0(\vec{k}) \\ & + \left. \left( \tilde{b}_{-2}(\vec{k}) + \frac{e^{i2\theta}}{2} \tilde{b}_0(\vec{k}) \right) \tilde{a}_2(\vec{k}) + \left( \frac{e^{i2\theta}}{2} \tilde{b}_{-2}(\vec{k}) \right) \right. \\ & \left. \tilde{a}_4(\vec{k}) \right] \end{aligned} \quad (4)$$

In pSIM, we change the direction of the illumination pattern 3 times ( $\theta_1 \sim \theta_3$ ), thus  $\tilde{a}_{-4}(\vec{k}) \sim \tilde{a}_4(\vec{k})$  can be retrieved by constructing a least-squares optimization with the Tikhonov

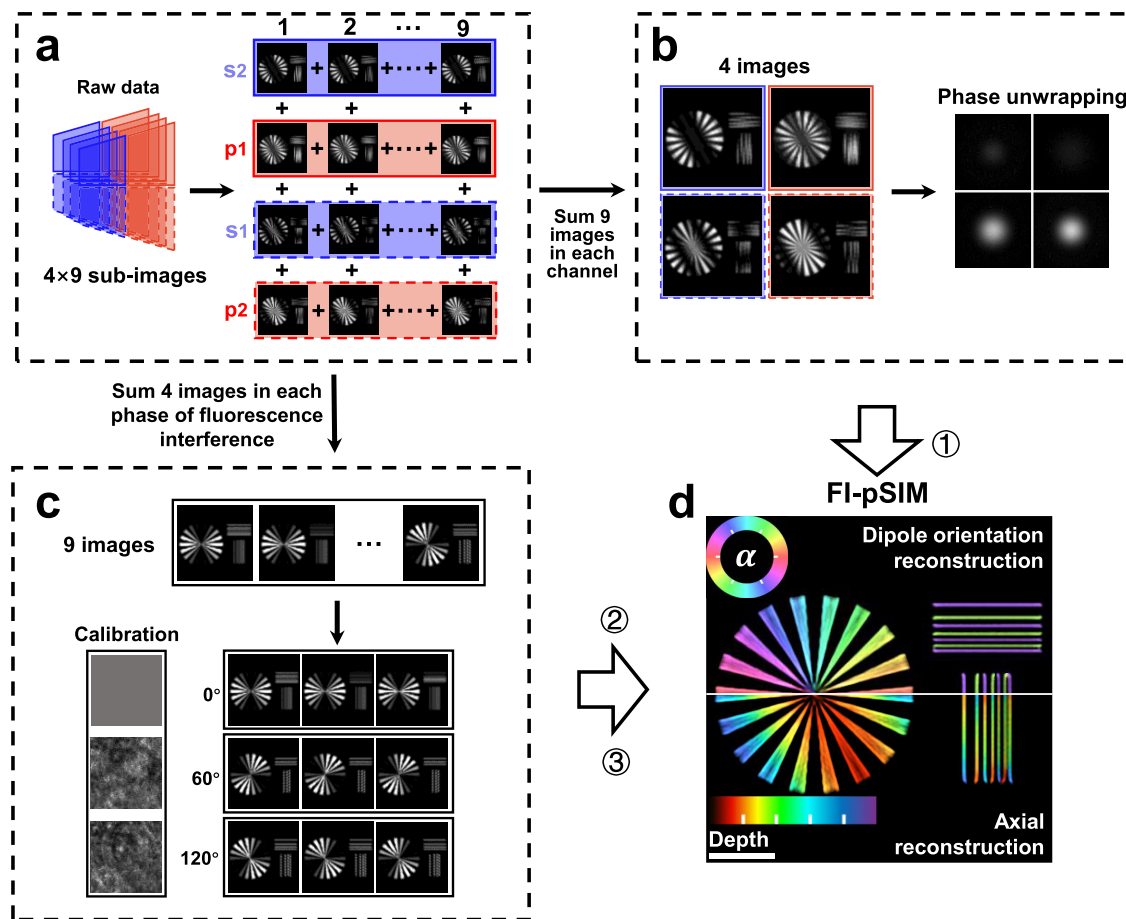


**Figure 2.** Pipeline of FI-pSIM. The process can be divided into axial reconstruction (①), dipole orientation reconstruction (②), and SIM reconstruction (③). (a) Camera is divided into 4 channels, and the raw data includes  $4 \times 9$  subimages. (b) Axial reconstruction process. (c) Dipole orientation reconstruction process. The role of calibration is to balance the illumination nonuniformity of each direction, which is discussed in detail in Notes S3 and S4 of Supporting Information. It should be noted that the SIM reconstruction process is also conducted in this process, and the SIM result can be used as a spatial mask for FI-pSIM image generation. (d) Final FI-pSIM image. Scale bar:  $2 \mu\text{m}$ .

regularization term.<sup>54</sup> High spatial frequency components  $B_{\theta,2}$  and  $B_{\theta,3}$  are also obtained

$$\begin{aligned}
 B_{\theta,2/3}(\vec{k}) = & 2\pi \left[ \left( \frac{e^{-i2\theta}}{2} \tilde{b}_2(\vec{k}) \right) \tilde{a}_{-4}(\vec{k} \pm \vec{k}_\theta) \right. \\
 & + \left( \tilde{b}_2(\vec{k}) + \frac{e^{-i2\theta}}{2} \tilde{b}_0(\vec{k}) \right) \tilde{a}_{-2}(\vec{k} \pm \vec{k}_\theta) \\
 & + \left( \frac{e^{i2\theta}}{2} \tilde{b}_2(\vec{k}) + \tilde{b}_0(\vec{k}) + \frac{e^{i2\theta}}{2} \tilde{b}_{-2}(\vec{k}) \right) \tilde{a}_0 \\
 & (\vec{k} \pm \vec{k}_\theta) + \left( \tilde{b}_{-2}(\vec{k}) + \frac{e^{i2\theta}}{2} \tilde{b}_0(\vec{k}) \right) \tilde{a}_2(\vec{k} \pm \vec{k}_\theta) \\
 & \left. + \left( \frac{e^{i2\theta}}{2} \tilde{b}_{-2}(\vec{k}) \right) \tilde{a}_4(\vec{k} \pm \vec{k}_\theta) \right] \quad (5)
 \end{aligned}$$

However, it is almost impossible to get  $\tilde{a}_{-4}(\vec{k} \pm \vec{k}_\theta) \sim \tilde{a}_4(\vec{k} \pm \vec{k}_\theta)$  through a single measurement. In practice, we did not try to get  $\tilde{a}_{-4}(\vec{k} \pm \vec{k}_\theta) \sim \tilde{a}_4(\vec{k} \pm \vec{k}_\theta)$  because the missing of them will not affect the estimation accuracy of the average azimuthal angle  $\alpha$ .<sup>28</sup> On the contrary, to achieve the super-resolution of the dipole concentration,  $B_{\theta,2}$  and  $B_{\theta,3}$  are moved back to their center frequency  $\pm \vec{k}_\theta$ . Combined with the HiFi-SIM recon-

struction algorithm,<sup>55</sup> a high-fidelity pSIM result can be reconstructed.

**Image Reconstruction Process.** To achieve both axial reconstruction and dipole orientation reconstruction, the entire image acquisition process is conducted on a home-built 4Pi wide-field microscope. In the excitation path, by the combination of galvo-mirror modules, single-axis piezo stage, and a customized pizza-shaped half-wave plate,<sup>50,56</sup> polarized structured illumination can be achieved with high modulation contrast with an ideal minimum extinction ratio for each excitation beam (better than 1:74). Comprehensive information is discussed in Note S5 of the Supporting Information. In this way, the linearly polarized excitation beams enter from the upper objective lens to form polarized structured illumination in three directions ( $0, 60, 120^\circ$ ) with three phase shifts of the excitation pattern in each direction (Figure 1a). In the detection path, through careful calibration of the phase difference between the four channels (Note S6 in the Supporting Information), the axial information can be encoded into the phase of fluorescence interference. To obtain the raw data of FI-pSIM, the camera is divided into four regions and collects images of fluorescence interference with different fluorescence phase shifts (Figure 2a). Finally, the raw data includes 9 images (36 subimages), including both axial information and dipole orientation information. In addition, the image registration of four

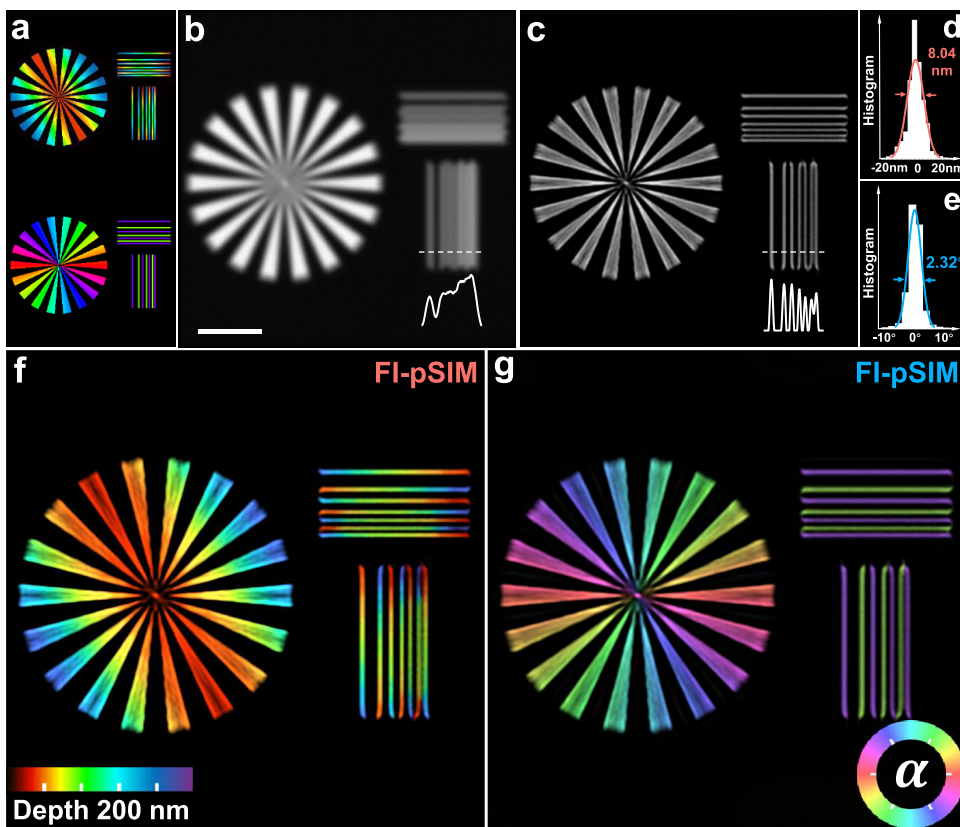


**Figure 3.** Simulation of FI-pSIM. (a) Ground truth of simulated data, which contains a star-like pattern and two groups of line pairs in the 240 nm axial range. In the star-like shape, the dipole azimuth angles are distributed radially along the circumference; in the line pairs, the dipole azimuth angles of adjacent straight lines are orthogonal ( $\frac{\pi}{4}$  and  $\frac{3\pi}{4}$ , respectively) and have opposite trends in axial distribution. Top: axial distribution with pseudo color; bottom: dipole orientation with pseudo color. (b) Wide-field (WF) image. The profile at the positions indicated by the white dashed line is displayed below. (c) SIM image. The profile at the positions indicated by the white dashed line is displayed below. (d) Frequency histogram of axial reconstruction error and fitting curve. (e) Frequency histogram of dipole orientation reconstruction error and fitting curve. (f) FI-pSIM result with a depth-coded 3D volume super-resolution image. (g) FI-pSIM result with a polarization-coded super-resolution image. Scale bar: 2  $\mu$ m.

subimages relies on a MATLAB toolbox “DIPimage” (<https://diplib.org/DIPimage.html>), which is widely used in image analysis of super-resolution microscopy.<sup>44,57,58</sup> DIPimage can help calculate the corresponding transformation matrix of each subimage so that each subimage matches with the others and can be used for the image reconstruction process.

The image reconstruction process of FI-pSIM includes two key steps: (i) dipole orientation reconstruction: calculating the ensemble dipole orientations and fluorophore density distributions (Figure 2c); and (ii) ensemble axial reconstruction of the sample (Figure 2b). Due to the fact that the fluorescence interference of four channels is independent of excitation and each channel follows the same rules in response to polarization excitation, summing the four channels up can obtain an image that is only modulated by polarized excitation, thus enabling the axial reconstruction by fluorescence interference and dipole orientation reconstruction by polarization to be independent in the data processing stage. As mentioned, the raw data of dipole orientation reconstruction is the sum of each subimage for every channel, and this summed-up raw data is first used to obtain the lateral super-resolution reconstruction of the fluorophore distribution and dipole orientation. Compared to a recently developed pSIM algorithm,<sup>28</sup> we have incorporated the most effective SIM algorithm developed most recently, i.e., HiFi-SIM<sup>55</sup> into the reconstruction process and obtained results with high fidelity (Figure 2c). It should be noted that the intensity

nonuniformity of each polarized illumination will affect the performance of dipole orientation reconstruction,<sup>28</sup> which can be precalibrated before reconstruction (Note S3 in Supporting Information). The super-resolved image (the same result as SIM) is then input into the axial reconstruction algorithm. When summing the 9 raw images of each channel, the four wide-field images that only reflect fluorescence interference results and are independent of the polarized excitation can be obtained. The SIM results at this time can be used as a spatial mask to obtain effective signals in each channel of the fluorescence interference (Figure 2b). By calculating the intensity distribution of the corresponding ROIs under different phases of fluorescence interference, the ensemble distribution of the sample in the axial direction can be obtained through the phase unwrapping process mentioned above.

Through the above steps, FI-pSIM can obtain 4D information on subcellular structures at a frame rate the same as that of SIM, including the three-dimensional distribution (same lateral resolution as SIM and sub-30 nm axial accuracy) and dipole orientation of the sample (Figure 2d).

**Simulations.** We first modeled the imaging process of FI-pSIM and conducted simulations for ensemble axial and dipole orientation reconstruction. By using vectorial diffraction theory,<sup>59–62</sup> the generated 4Pi-PSFs with different phases can closely match the experimental situation under the high NA condition.

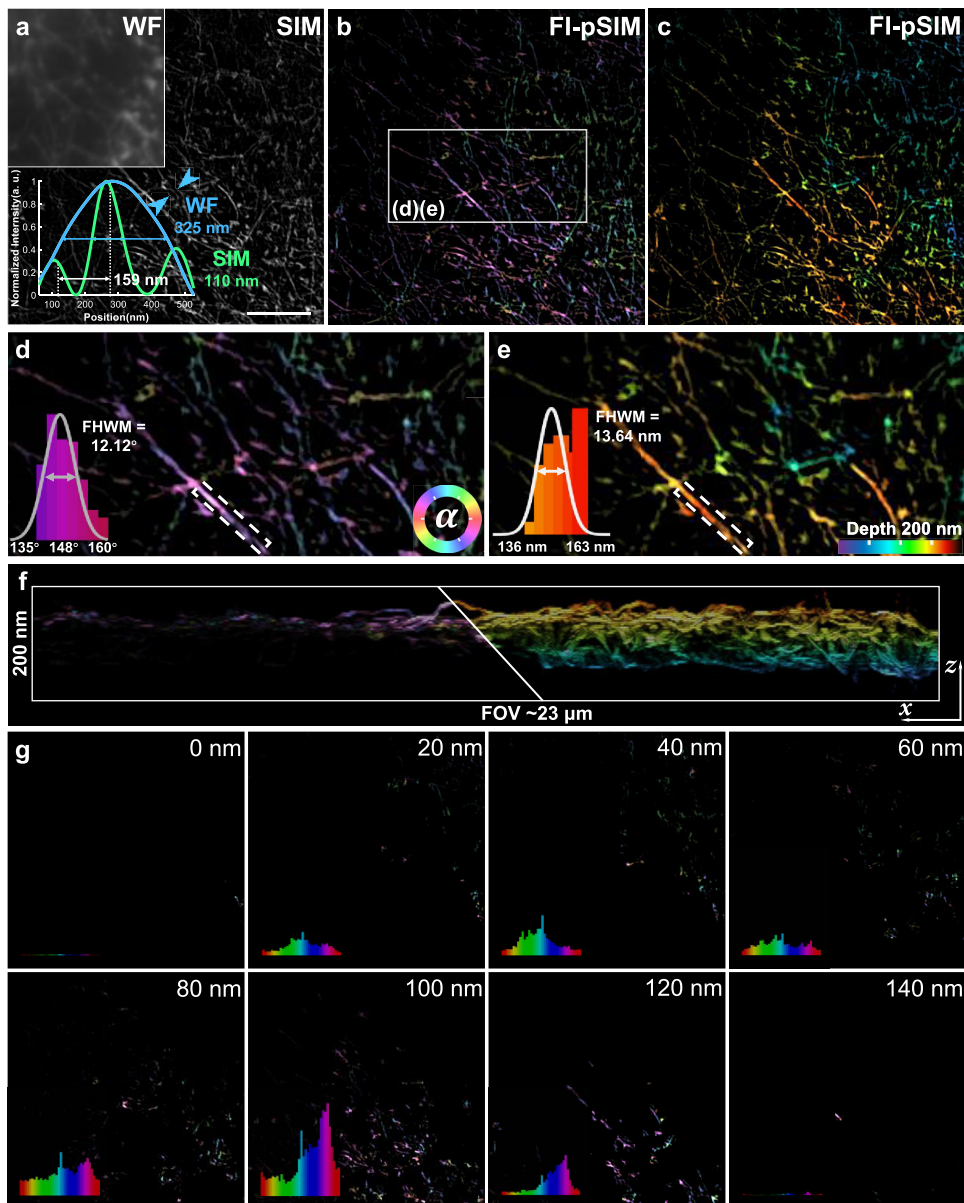


**Figure 4.** FI-pSIM results of fixed actin filaments labeled with Alexa Fluor 488-phalloidin. (a) SIM image. The top-left of (a) is the corresponding wide-field image of the top-left part of the whole field of view. The blue and green curves are lateral profiles of wide-field image and SIM image of the position indicated by blue arrows and the FWHMs are 325 and 110 nm, respectively. The distance between the two peaks on the left side of the SIM profile is 159 nm, indicating that the lateral resolution of FI-pSIM is better than that at 159 nm. (b) FI-pSIM result with a polarization-coded super-resolution image. (c) FI-pSIM result with a depth-coded 3D volume super-resolution image. (d) Polarization-coded super-resolution image marked in (b). The histogram reveals the dipole orientation in the region of interest, marked by a white dashed box. The average direction of actin filaments in the box is 140°, while the average reconstructed dipole orientation is 147.93°, with a FWHM of 12.12°. And the color of the histogram matches the angle represented by the color wheel. (e) Depth-coded super-resolution image marked in (b). The histogram denotes the depth distribution in the region of interest, marked by a white dashed box. The average reconstructed depth of actin filaments in the box is 152.42 nm, with a FWHM of 13.64 nm. (f)  $x-z$  section of FI-pSIM result. Left:  $x-z$  section of polarization-coded super-resolution image; Right:  $x-z$  section of depth-coded super-resolution image. The actin filaments are distributed in a space of  $23\ \mu\text{m} \times 23\ \mu\text{m} \times 200\ \text{nm}$ . (g) Continuous  $x-y$  section of the 3D volume from 0 to 140 nm depth with a 20 nm axial interval, illustrating the changing morphology and dipole orientations of microtubule networks. The histogram of dipole distribution from each  $x-y$  section is shown in (f). Scale bar: 5  $\mu\text{m}$ .

As illustrated in Figure 3a, the simulated 3D sample with a star-like shape and two groups of line pairs with different spacing are reconstructed through FI-pSIM. The pixel size is set to 30 nm, the emission wavelength is 585 nm, and NA is set to 1.45. To reflect the spatial information, the axial range of the simulation data is set to 240 nm. For the line pairs, the dipole orientations between adjacent straight lines are orthogonal ( $\frac{\pi}{4}$

and  $\frac{3\pi}{4}$ , respectively) and the axial morphologies are opposite. The lateral spacing between line pairs from left to right (the other group is from top to bottom) is 300, 150, 150, 90, 90, and 60 nm, respectively. For the star-like shape, the dipole azimuth angles distributed radially along the circumference. In the process of axial reconstruction, the axial information is displayed as a pseudo color and the depth is coded into colors from warm to cold. As shown in Figure 3f,g, the 3D sample is fully recovered

by SIM and axial reconstruction from 4Pi four-channel detection. The standard deviation of the axial error is 8.04 nm from the ground truth (Figure 3d), and the error of all reconstructed ROIs does not exceed 15 nm, which indicates that FI-pSIM guarantees axial accuracy better than 30 and even 15 nm. Certainly, simulation cannot fully reflect the actual imaging process. To further validate the axial reconstruction performance of FI-pSIM, single-layer 100 nm fluorescent beads (Note S9 in the Supporting Information) were used to measure the accuracy of axial reconstruction. From Note S7 in the Supporting Information, it can be observed that within a FOV of 22  $\mu\text{m}$ , the axial distribution of fluorescent beads is close to a horizontal plane at 0 nm in the axial direction, and the worst accuracy remains at sub-20 nm. This result proves that the axial reconstruction performance of FI-pSIM is consistent with simulation. In the meantime, the dipole orientation is also reconstructed, displayed as a pseudo color that corresponds to the color wheel (Figure 3g). The reconstructed ensemble dipole orientation is consistent with the ground truth, and the standard deviation of the orientation error is about 2.32° (Figure 3e). The impact of different parameters in the imaging process on ensemble dipole orientation reconstruction has also been further discussed in Note S8 in the Supporting Information. The simulation results indicate that although the straight lines with a lateral spacing of 60 nm cannot be completely separated (Figure 3b,c), FI-pSIM can synchronously reconstruct the 3D distribution and dipole orientation of the sample, while improving lateral resolution to 100 nm and achieving axial reconstruction with sub-30 nm accuracy.

**Experiments.** To further validate the performance of FI-pSIM, we conducted biological experiments. As illustrated in Figure 4, Fixed actin filaments of BSC cells are labeled by Alexa Fluor 488-phalloidin (Note S9 in the Supporting Information) and excited by a 488 nm laser (MPB Communications, 2RU-VFL-P-500-488-B1R) under polarized structured illumination. To ensure the effectiveness of modulation contrast, the laser power density should remain constant (around 1–10W/cm<sup>2</sup>) to prevent overexposure during the image acquisition procedure. Combined with calibration maps (Notes S3 and S4 in the Supporting Information), the influence of nonuniform illumination can be avoided. During the reconstruction process of HiFi-SIM, to reduce artifacts caused by defocusing and background information due to applying dual objective lenses, the damping factor value  $\beta$  was set to 0.4 and the value of OTF attention strength was set to 0.95 empirically.<sup>55</sup>

Through FI-pSIM, the 3D morphological image of actin filaments can be displayed with a 3D super-resolution and dipole orientation. While maintaining the lateral resolution of SIM the full width at half-maximum (FWHM) at the blue arrow in Figure 4a is around 110 nm. As a comparison, the counterpart of wide-field image (WF) is 325 nm because the filaments with a minimum spacing of 159 nm cannot be distinguished; the axial distributions of the actin filaments can be revealed. The structure of actin filaments in the field of view (FOV) of 23  $\mu\text{m}$  is roughly divided into two layers (bottom and right of Figure 4c, respectively), and the histogram shows an average depth of 152.42 nm with a FWHM of 13.64 nm (Figure 4e). At the same time as the axial distribution is obtained, the dipole orientations are also reconstructed successfully (Figure 4b). It can be clearly shown that the ensemble dipole orientations are nearly parallel to the direction of the actin filaments itself in the lateral direction. There exists an 8° deviation between the actin filaments direction and reconstructed dipole orientation (Figure

4d), which is consistent with previously reported values.<sup>28</sup> Using FI-pSIM, the 4D image (Figure 4fg), which includes 3D distribution and polarization information with a histogram of dipole orientation for each axial layer, can be displayed by just collecting only one group of images (9 images for each channel).

## ■ DISCUSSION AND CONCLUSIONS

Through polarization demodulation and fluorescence interference, FI-pSIM achieves 4D imaging with a high axial accuracy of sub-30 nm by collecting only 9 raw images (36 subimages). By conducting fixed-cell experiments, we have validated the feasibility and performance of our theory and hardware. We believe that FI-pSIM will provide new tools for exploring the activity mechanisms in four dimensions of  $x$ ,  $y$ ,  $z$ , and polarization. It will also assist in deciphering the interactions between various matter and structure in life science in the future. The low power density of FI-pSIM also has the potential for live-cell imaging, as reported in previous research based on a single objective lens.<sup>28,35</sup> However, the special sample preparation process of the 4Pi configuration (Note S9 in the Supporting Information) results in very little liquid in the sample, affecting cell activity and fluorescence intensity. Especially for live-cell samples with polarization characteristics labeled with covalent probes or green fluorescent protein, obtaining polarization information remains a challenge.

It is worth noting that the axial reconstruction accuracy of FI-pSIM is typically much higher than its lateral resolution; however, achieving isotropic resolution is a significant topic in microscopic imaging. To align the lateral resolution of FI-pSIM with its axial reconstruction accuracy, one promising approach is to integrate FI-pSIM with nonlinear intensity modulation, achieved through the reversible photoswitching of a fluorescent protein.<sup>32,63</sup> This integration is expected to enhance the lateral resolution to below 50 nm without increasing the phototoxicity.

It is also worth discussing that under ensemble conditions, ensuring the axial and angular accuracy of reconstructing densely overlapping parts of the sample is difficult due to the fact that ensemble reconstruction is derived from wide-field images, where all fluorescent molecules emit fluorescence simultaneously. Meanwhile, due to convolution with PSF, the calculated dipole orientation cannot fully reflect the practical condition in the sample (Notes S1 and S2 in Supporting Information). Therefore, obtaining a better dipole orientation distribution through solving the optimization problem will be the research topic in the next stage. There is still room for improving the axial detection range.

Improving the accuracy of ensemble dipole orientation reconstruction is crucial for polarization microscopy. Modulating the polarization state of fluorescence at the detection path is a feasible method,<sup>64</sup> but it will affect the accuracy of axial reconstruction. How to improve the accuracy of dipole orientation reconstruction while maintaining the existing axial accuracy is a promising research direction. And it is also an important topic to obtain complete 3D dipole orientation information, both azimuthal angle and polar angle, while maintaining the spatial super-resolution capability. Rimoli et al.<sup>65</sup> used a combination of a PBS and a half-wave plate (HWP), along with a smaller NA, to obtain the 2D orientation and wobble angles of dipoles while maintaining the Gaussian shape of the PSF. Wu et al.<sup>66</sup> achieved high-precision 3D dipole orientation and wobble angle by combining optimization algorithm with polarized splitting of fluorescence. Similar

methods can be combined with the fluorescence interference module for additional axial morphology super-resolution.

Although the axial detection range can be extended through phase unwrapping, it cannot reconstruct thick samples with discontinuous distributions. Combining adaptive optics for reconstructing thick samples will also be a future research direction. We must also acknowledge that to exhibit polarity in fluorophore, labeling strategies such as using rigidly linked green fluorescent protein and small-molecule probe tags are required. Meanwhile, the 4Pi configuration requires the sample to be sealed between two coverslips<sup>44</sup> which inevitably reduces the activity and lifespan of the sample. Optimizing the labeling strategy and sealing method will be beneficial for improving the performance of FI-pSIM. In terms of algorithms, integrating faster spatial domain reconstruction methods for real-time reconstruction<sup>67,68</sup> could greatly reduce the time spent searching for target structures, thus mitigating the issue of short viability in live-cell samples.

## ■ ASSOCIATED CONTENT

### SI Supporting Information

The Supporting Information is available free of charge at <https://pubs.acs.org/doi/10.1021/acsphtronics.4c01807>.

Principal derivation; dipole point spread function; calibration process of illumination nonuniformity; time-varying change of calibration map; process of polarization modulation; calibration process of fluorescence interference phase difference; axial reconstruction accuracy of FI-pSIM; influences factor of ensemble dipole orientation reconstruction accuracy and sample preparation ([PDF](#))

## ■ AUTHOR INFORMATION

### Corresponding Author

Cuifang Kuang – State Key Laboratory of Extreme Photonics and Instrumentation, College of Optical Science and Engineering, Zhejiang University, Hangzhou, Zhejiang 310027, China; ZJU-Hangzhou Global Scientific and Technological Innovation Center, Hangzhou, Zhejiang 311200, China; Collaborative Innovation Center of Extreme Optics, Shanxi University, Taiyuan, Shanxi 030006, China; [orcid.org/0000-0002-7650-0349](#); Email: [cukuang@zju.edu.cn](mailto:cukuang@zju.edu.cn)

### Authors

Yile Sun – State Key Laboratory of Extreme Photonics and Instrumentation, College of Optical Science and Engineering, Zhejiang University, Hangzhou, Zhejiang 310027, China

Hongfei Zhu – Department of Biomedical Engineering, The Chinese University of Hong Kong, Shatin, Hong Kong 999077, China

Xinxun Yang – State Key Laboratory of Extreme Photonics and Instrumentation, College of Optical Science and Engineering, Zhejiang University, Hangzhou, Zhejiang 310027, China

Enxing He – State Key Laboratory of Extreme Photonics and Instrumentation, College of Optical Science and Engineering, Zhejiang University, Hangzhou, Zhejiang 310027, China

Hanmeng Wu – State Key Laboratory of Extreme Photonics and Instrumentation, College of Optical Science and Engineering, Zhejiang University, Hangzhou, Zhejiang 310027, China

Lu Yin – College of Optical and Electronic Technology, China Jiliang University, Hangzhou, Zhejiang 310018, China

Weiyun Sun – Institute of Pharmacology, College of Pharmaceutical Sciences, Zhejiang University of Technology, Hangzhou, Zhejiang 310014, China

Xin Luo – State Key Laboratory of Extreme Photonics and Instrumentation, College of Optical Science and Engineering, Zhejiang University, Hangzhou, Zhejiang 310027, China

Yubing Han – State Key Laboratory of Extreme Photonics and Instrumentation, College of Optical Science and Engineering, Zhejiang University, Hangzhou, Zhejiang 310027, China

Xiang Hao – State Key Laboratory of Extreme Photonics and Instrumentation, College of Optical Science and Engineering, Zhejiang University, Hangzhou, Zhejiang 310027, China; [orcid.org/0000-0002-3931-6884](#)

Renjie Zhou – Department of Biomedical Engineering, The Chinese University of Hong Kong, Shatin, Hong Kong 999077, China; [orcid.org/0000-0002-4761-6641](#)

Xu Liu – State Key Laboratory of Extreme Photonics and Instrumentation, College of Optical Science and Engineering, Zhejiang University, Hangzhou, Zhejiang 310027, China; ZJU-Hangzhou Global Scientific and Technological Innovation Center, Hangzhou, Zhejiang 311200, China; Collaborative Innovation Center of Extreme Optics, Shanxi University, Taiyuan, Shanxi 030006, China

Complete contact information is available at:

<https://pubs.acs.org/10.1021/acsphtronics.4c01807>

### Author Contributions

Y.S. and H.Z. contributed equally to this work. Y.S. and H.Z. contributed to conceptualization, formal analysis, investigation, methodology, visualization, validation, writing—original draft. X.Y., E.H., H.W., and L.Y. contributed to formal analysis, investigation, methodology. X.L., W.S., and Y.H. contributed to investigation and methodology. R.Z. contributed to supervision, writing—review and editing. X.H. and X.L. contributed to supervision. C.K. contributed to conceptualization, funding acquisition, supervision, project administration, writing—review and editing.

### Funding

This work was financially sponsored by the National Natural Science Foundation of China (62361166631, 62125504); STI 2030—Major Projects (2021ZD0200401); the Fundamental Research Funds for the Central Universities (2022FZZX01–20, 226–2022–00201).

### Notes

The authors declare no competing financial interest.

## ■ REFERENCES

- (1) Betzig, E.; Patterson, G. H.; Sougrat, R.; Lindwasser, O. W.; Olenych, S.; Bonifacino, J. S.; Davidson, M. W.; Lippincott-Schwartz, J.; Hess, H. F. Imaging Intracellular Fluorescent Proteins at Nanometer Resolution. *Science* **2006**, *313* (5793), 1642–1645.
- (2) Rust, M. J.; Bates, M.; Zhuang, X. Sub-Diffraction-Limit Imaging by Stochastic Optical Reconstruction Microscopy (STORM). *Nat. Methods* **2006**, *3* (10), 793–796.
- (3) Gustafsson, M. G. L. Surpassing the Lateral Resolution Limit by a Factor of Two Using Structured Illumination Microscopy. *J. Microsc.* **2000**, *198* (2), 82–87.
- (4) Hell, S. W.; Wichmann, J. Breaking the Diffraction Resolution Limit by Stimulated Emission: Stimulated-Emission-Depletion Fluorescence Microscopy. *Opt. Lett.* **1994**, *19* (11), 780–782.
- (5) Sigal, Y. M.; Zhou, R.; Zhuang, X. Visualizing and Discovering Cellular Structures with Super-Resolution Microscopy. *Science* **2018**, *361* (6405), 880–887.

- (6) Gu, L.; Li, Y.; Zhang, S.; Xue, Y.; Li, W.; Li, D.; Xu, T.; Ji, W. Molecular Resolution Imaging by Repetitive Optical Selective Exposure. *Nat. Methods* **2019**, *16* (11), 1114–1118.
- (7) Cnossen, J.; Hinsdale, T.; Thorsen, R. Ø.; Siemons, M.; Schueder, F.; Jungmann, R.; Smith, C. S.; Rieger, B.; Stallinga, S. Localization Microscopy at Doubled Precision with Patterned Illumination. *Nat. Methods* **2020**, *17* (1), 59–63.
- (8) Reymond, L.; Ziegler, J.; Knapp, C.; Wang, F.-C.; Huser, T.; et al. SIMPLE: Structured Illumination Based Point Localization Estimator with Enhanced Precision. *Opt. Express* **2019**, *27* (17), 24578–24590.
- (9) van Velde, P.; Rieger, B.; Hinsdale, T.; Cnossen, J.; Fan, D.; Hung, S.-T.; Grunwald, D.; Smith, C. ZIMFLUX: Single Molecule Localization Microscopy with Patterned Illumination in 3D. *Opt. Express* **2023**, *31* (25), 42701–42722.
- (10) Sun, Y.; Yin, L.; Cai, M.; Wu, H.; Hao, X.; Kuang, C.; Liu, X. Modulated Illumination Localization Microscopy-Enabled Sub-10 nm Resolution. *J. Innovative Opt. Health Sci.* **2022**, *15* (02), No. 2230004.
- (11) Reinhardt, S. C. M.; Masullo, L. A.; Baudrexel, I.; Steen, P. R.; Kowalewski, R.; Eklund, A. S.; Strauss, S.; Unterauer, E. M.; Schlüchthaerle, T.; Strauss, M. T.; Klein, C.; Jungmann, R. Ångström-Resolution Fluorescence Microscopy. *Nature* **2023**, *617* (7962), 711–716.
- (12) Weber, M.; von der Emde, H.; Leutenegger, M.; Gunkel, P.; Sambandan, S.; Khan, T. A.; Keller-Findeisen, J.; Cordes, V. C.; Hell, S. W. MINSTED Nanoscopy Enters the Ångström Localization Range. *Nat. Biotechnol.* **2023**, *41*, 569–576.
- (13) Brasselet, S.; Alonso, M. A. Polarization Microscopy: From Ensemble Structural Imaging to Single-Molecule 3D Orientation and Localization Microscopy. *Optica* **2023**, *10* (11), 1486–1510.
- (14) Chandler, T.; Shroff, H.; Oldenbourg, R.; Rivière, P. L. Spatio-Angular Fluorescence Microscopy I. Basic Theory. *J. Opt. Soc. Am. A* **2019**, *36* (8), 1334–1345.
- (15) Chandler, T.; Shroff, H.; Oldenbourg, R.; Rivière, P. L. Spatio-Angular Fluorescence Microscopy II. Paraxial 4f Imaging. *J. Opt. Soc. Am. A* **2019**, *36* (8), 1346–1360.
- (16) Chandler, T.; Shroff, H.; Oldenbourg, R.; Rivière, P. L. Spatio-Angular Fluorescence Microscopy III. Constrained Angular Diffusion, Polarized Excitation, and High-NA Imaging. *J. Opt. Soc. Am. A* **2020**, *37* (9), 1465–1479.
- (17) Ha, T.; Enderlein, T.; Chemla, D. S.; Selvin, P. R.; Weiss, S. Single Molecule Dynamics Studied by Polarization Modulation. *Phys. Rev. Lett.* **1996**, *77* (19), 3979–3982.
- (18) Enderlein, J.; Toprak, E.; Selvin, P. R. Polarization Effect on Position Accuracy of Fluorophore Localization. *Opt. Express* **2006**, *14* (18), 8111–8120.
- (19) Mortensen, K. I.; Churchman, L. S.; Spudich, J. A.; Flyvbjerg, H. Optimized Localization Analysis for Single-Molecule Tracking and Super-Resolution Microscopy. *Nat. Methods* **2010**, *7* (5), 377–381.
- (20) Backlund, M. P.; Lew, M. D.; Backer, A. S.; Sahl, S. J.; Grover, G.; Agrawal, A.; Piestun, R.; Moerner, W. E. Simultaneous, Accurate Measurement of the 3D Position and Orientation of Single Molecules. *Proc. Natl. Acad. Sci. U.S.A.* **2012**, *109* (47), 19087–19092.
- (21) Nevskyi, O.; Tsukanov, R.; Gregor, I.; Karedla, N.; Enderlein, J. Fluorescence Polarization Filtering for Accurate Single Molecule Localization. *APL Photonics* **2020**, *5* (6), No. 061302.
- (22) Thorsen, R. Ø.; Hulleman, C. N.; Rieger, B.; Stallinga, S. Photon Efficient Orientation Estimation Using Polarization Modulation in Single-Molecule Localization Microscopy. *Biomed. Opt. Express* **2022**, *13* (5), 2835–2858.
- (23) Zhang, O.; Guo, Z.; He, Y.; Wu, T.; Vahey, M. D.; Lew, M. D. Six-Dimensional Single-Molecule Imaging with Isotropic Resolution Using a Multi-View Reflector Microscope. *Nat. Photonics* **2023**, *17* (2), 179–186.
- (24) Backer, A. S.; Lee, M. Y.; Moerner, W. E. Enhanced DNA Imaging Using Super-Resolution Microscopy and Simultaneous Single-Molecule Orientation Measurements. *Optica* **2016**, *3* (6), 659–666.
- (25) Zhang, O.; Lew, M. D. Fundamental Limits on Measuring the Rotational Constraint of Single Molecules Using Fluorescence Microscopy. *Phys. Rev. Lett.* **2019**, *122* (19), No. 198301.
- (26) Zhou, W.; Wu, T.; Lew, M. D. Fundamental Limits in Measuring the Anisotropic Rotational Diffusion of Single Molecules. *J. Phys. Chem. A* **2024**, *128* (28), 5808–5815.
- (27) Zhang, O.; Lew, M. D. Single-Molecule Orientation Localization Microscopy I: Fundamental Limits. *J. Opt. Soc. Am. A* **2021**, *38* (2), 277–287.
- (28) Zhanghao, K.; Chen, X.; Liu, W.; Li, M.; Liu, Y.; Wang, Y.; Luo, S.; Wang, X.; Shan, C.; Xie, H.; Gao, J.; Chen, X.; Jin, D.; Li, X.; Zhang, Y.; Dai, Q.; Xi, P. Super-Resolution Imaging of Fluorescent Dipoles via Polarized Structured Illumination Microscopy. *Nat. Commun.* **2019**, *10* (1), No. 4694.
- (29) Lelek, M.; Gyparaki, M. T.; Beliu, G.; Schueder, F.; Griffié, J.; Manley, S.; Jungmann, R.; Sauer, M.; Lakadamyali, M.; Zimmer, C. Single-Molecule Localization Microscopy. *Nat. Rev. Methods Primers* **2021**, *1* (1), No. 39.
- (30) Hafi, N.; Grunwald, M.; van den Heuvel, L. S.; Aspelmeier, T.; Chen, J.-H.; Zagrebelsky, M.; Schütte, O. M.; Steinem, C.; Korte, M.; Munk, A.; Walla, P. J. Fluorescence Nanoscopy by Polarization Modulation and Polarization Angle Narrowing. *Nat. Methods* **2014**, *11* (5), 579–584.
- (31) Zhanghao, K.; Chen, L.; Yang, X.-S.; Wang, M.-Y.; Jing, Z.-L.; Han, H.-B.; Zhang, M. Q.; Jin, D.; Gao, J.-T.; Xi, P. Super-Resolution Dipole Orientation Mapping via Polarization Demodulation. *Light: Sci. Appl.* **2016**, *5* (10), No. e16166.
- (32) Li, D.; Shao, L.; Chen, B.-C.; Zhang, X.; Zhang, M.; Moses, B.; Milkie, D. E.; Beach, J. R.; Hammer, J. A.; Pasham, M.; Kirchhausen, T.; Baird, M. A.; Davidson, M. W.; Xu, P.; Betzig, E. Extended-Resolution Structured Illumination Imaging of Endocytic and Cytoskeletal Dynamics. *Science* **2015**, *349* (6251), No. aab3500.
- (33) Gustafsson, M. G.; Shao, L.; Carlton, P. M.; Wang, C. R.; Golubovskaya, I. N.; Cande, W. Z.; Agard, D. A.; Sedat, J. W. Three-Dimensional Resolution Doubling in Wide-Field Fluorescence Microscopy by Structured Illumination. *Biophys. J.* **2008**, *94* (12), 4957–4970.
- (34) Li, Y.; Cao, R.; Ren, W.; Fu, Y.; Hou, Y.; Zhong, S.; Zhanghao, K.; Li, M.; Xi, P. High-Speed Autopolarization Synchronization Modulation Three-Dimensional Structured Illumination Microscopy. *Adv. Photonics Nexus* **2024**, *3* (1), No. 016001.
- (35) Cao, R.; Li, Y.; Chen, X.; Ge, X.; Li, M.; Guan, M.; Hou, Y.; Fu, Y.; Xu, X.; Jiang, S.; Gao, B.; Xi, P. Open-3DSIM: An Open-Source Three-Dimensional Structured Illumination Microscopy Reconstruction Platform. *Nat. Methods* **2023**, DOI: [10.1038/s41592-023-01958-0](https://doi.org/10.1038/s41592-023-01958-0).
- (36) Schön, P.; Behrndt, M.; Aït-Belkacem, D.; Rigneault, H.; Brasselet, S. Polarization and Phase Pulse Shaping Applied to Structural Contrast in Nonlinear Microscopy Imaging. *Phys. Rev. A* **2010**, *81* (1), No. 013809.
- (37) Hall, N.; Dobbie, I. Structured Illumination Microscopy. In *Principles of Light Microscopy: From Basic to Advanced*; Nechyporuk-Zloy, V., Ed.; Springer International Publishing: Cham, 2022; pp 173–194.
- (38) Chen, X.; Zhong, S.; Hou, Y.; Cao, R.; Wang, W.; Li, D.; Dai, Q.; Kim, D.; Xi, P. Superresolution Structured Illumination Microscopy Reconstruction Algorithms: A Review. *Light: Sci. Appl.* **2023**, *12* (1), No. 172.
- (39) Shao, L.; Isaac, B.; Uzawa, S.; Agard, D. A.; Sedat, J. W.; Gustafsson, M. G. L. ISS: Wide-Field Light Microscopy with 100-nm-Scale Resolution in Three Dimensions. *Biophys. J.* **2008**, *94* (12), 4971–4983.
- (40) Chen, Y.; Liu, W.; Zhang, Z.; Zheng, C.; Huang, Y.; Cao, R.; Zhu, D.; Xu, L.; Zhang, M.; Zhang, Y.-H.; et al. Multi-Color Live-Cell Super-Resolution Volume Imaging with Multi-Angle Interference Microscopy. *Nat. Commun.* **2018**, *9* (1), No. 4818.
- (41) Manton, J. D.; Ströhl, F.; Fiolka, R.; Kaminski, C. F.; Rees, E. J. Concepts for Structured Illumination Microscopy with Extended Axial Resolution through Mirrored Illumination. *Biomed. Opt. Express* **2020**, *11* (4), 2098–2108.
- (42) Li, X.; Wu, Y.; Su, Y.; Rey-Suarez, I.; Matthaeus, C.; Updegrove, T. B.; Wei, Z.; Zhang, L.; Sasaki, H.; Li, Y.; Guo, M.; Giannini, J. P.; Vishwasrao, H. D.; Chen, J.; Lee, S.-J.; Shao, L.; Liu, H.; Ramamurthy,

- K. S.; Taraska, J. W.; Upadhyaya, A.; La Riviere, P.; Shroff, H. Three-Dimensional Structured Illumination Microscopy with Enhanced Axial Resolution. *Nat. Biotechnol.* **2023**, *41*, 1307–1319.
- (43) Boland, M. A.; Cohen, E. A. K.; Flaxman, S. R.; Neil, M. A. A. Improving Axial Resolution in Structured Illumination Microscopy Using Deep Learning. *Philos. Trans. R. Soc., A* **2021**, *379* (2199), No. 20200298.
- (44) Wang, J.; Allgeyer, E. S.; Sirinakis, G.; Zhang, Y.; Bewersdorf, J.; et al. Implementation of a 4Pi-SMS Super-Resolution Microscope. *Nat. Protoc.* **2021**, *16*, 677–727, DOI: 10.1038/s41596-020-00428-7.
- (45) Bilanca, A.; Cao, J.; Colice, M.; Ozcan, A.; Bouma, B.; Raftery, L.; Tearney, G. Fluorescence Interferometry: Principles and Applications in Biology. *Ann. N.Y. Acad. Sci.* **2008**, *1130*, 68–77.
- (46) Aquino, D.; Schönle, A.; Geisler, C.; v Middendorff, C.; Wurm, C. A.; Okamura, Y.; Lang, T.; Hell, S. W.; Egner, A. Two-Color Nanoscopy of Three-Dimensional Volumes by 4Pi Detection of Stochastically Switched Fluorophores. *Nat. Methods* **2011**, *8* (4), 353–359.
- (47) Gustafsson, M. G. L.; Agard, D. A.; Sedat, J. W. Sevenfold Improvement of Axial Resolution in 3D Wide-Field Microscopy Using Two Objective Lenses, Proceedings of SPIE—The International Society for Optical Engineering; SPIE, 1995; pp 147–156.
- (48) Gustafsson, M. G. L.; Agard, D. A.; Sedat, J. W. ISM: 3D Widefield Light Microscopy with Better than 100 nm Axial Resolution. *J. Microsc.* **1999**, *195* (Pt 1), 10–16.
- (49) Hell, S. W.; Schmidt, R.; Egner, A. Diffraction-Unlimited Three-Dimensional Optical Nanoscopy with Opposing Lenses. *Nat. Photonics* **2009**, *3* (7), 381–387.
- (50) Sun, Y.; Zhu, H.; Yin, L.; Wu, H.; Cai, M.; Sun, W.; Xu, Y.; Yang, X.; Han, J.; Liu, W.; Han, Y.; Hao, X.; Zhou, R.; Kuang, C.; Liu, X. Fluorescence Interference Structured Illumination Microscopy for 3D Morphology Imaging with High Axial Resolution. *Adv. Photonics* **2023**, *5* (5), No. 056007.
- (51) Bates, M.; Keller-Findeisen, J.; Przybylski, A.; Hüper, A.; Stephan, T.; Ilgen, P.; Delgado, A. R. C.; D'Este, E.; Jakobs, S.; Sahl, S. J.; et al. Optimal Precision and Accuracy in 4Pi-STORM Using Dynamic Spline PSF Models. *Nat. Methods* **2022**, *19*, 603–612.
- (52) Liu, W.; Liu, Q.; Zhang, Z.; Han, Y.; Kuang, C.; Xu, L.; Yang, H.; Liu, X. Three-Dimensional Super-Resolution Imaging of Live Whole Cells Using Galvanometer-Based Structured Illumination Microscopy. *Opt. Express* **2019**, *27* (5), 7237–7248.
- (53) Ferrand, P.; Gasecka, P.; Kress, A.; Wang, X.; Bioud, F.-Z.; Duboisset, J.; Brasselet, S. Ultimate Use of Two-Photon Fluorescence Microscopy to Map Orientational Behavior of Fluorophores. *Biophys. J.* **2014**, *106* (11), 2330–2339.
- (54) Chandler, T.; Guo, M.; Su, Y.; Chen, J.; Wu, Y.; Liu, J.; Agashe, A.; Fischer, R. S.; Mehta, S. B.; Kumar, A.; Baskin, T. I.; Jamouille, V.; Liu, H.; Swaminathan, V.; Nain, A.; Oldenbourg, R.; Rivière, P. L.; Shroff, H. Three-Dimensional Spatio-Angular Fluorescence Microscopy with a Polarized Dual-View Inverted Selective-Plane Illumination Microscope (Pol-diSPIM). *bioRxiv* **2024**, DOI: 10.1101/2024.03.09.584243.
- (55) Wen, G.; Li, S.; Wang, L.; Chen, X.; Li, H.; et al. High-Fidelity Structured Illumination Microscopy by Point-Spread-Function Engineering. *Light: Sci. Appl.* **2021**, *10* (1), No. 70.
- (56) Wu, H.; Li, Y.; Sun, Y.; Yin, L.; Sun, W.; Ye, Z.; Yang, X.; Zhu, H.; Tang, M.; Han, Y.; Kuang, C.; Liu, X. Single-Frame Structured Illumination Microscopy for Fast Live-Cell Imaging. *APL Photonics* **2024**, *9* (3), No. 036102.
- (57) Huang, F.; Sirinakis, G.; Allgeyer, E. S.; Schroeder, L. K.; Duim, W. C.; Kromann, E. B.; Phan, T.; Rivera-Molina, F. E.; Myers, J. R.; Irnov, I.; Lessard, M.; Zhang, Y.; Handel, M. A.; Jacobs-Wagner, C.; Lusk, C. P.; Rothman, J. E.; Toomre, D.; Booth, M. J.; Bewersdorf, J. Ultra-High Resolution 3D Imaging of Whole Cells. *Cell* **2016**, *166* (4), 1028–1040.
- (58) Zhang, Y.; Schroeder, L. K.; Lessard, M. D.; Kidd, P.; Chung, J.; Song, Y.; Benedetti, L.; Li, Y.; Ries, J.; Grimm, J. B.; Lavis, L. D.; De Camilli, P.; Rothman, J. E.; Baddeley, D.; Bewersdorf, J. Nanoscale Subcellular Architecture Revealed by Multicolor Three-Dimensional Salvaged Fluorescence Imaging. *Nat. Methods* **2020**, *17* (2), 225–231.
- (59) Wolf, E. Electromagnetic Diffraction in Optical Systems-I. An Integral Representation of the Image Field. *Proc. R. Soc. London, Ser. A* **1959**, *253* (1274), 349–357.
- (60) Hao, X.; Allgeyer, E. S.; Booth, M. J.; Bewersdorf, J. Point-Spread Function Optimization in isoSTED Nanoscopy. *Opt. Lett.* **2015**, *40* (15), 3627–3630.
- (61) Li, Y.; Buglakova, E.; Zhang, Y.; Thevathasan, J. V.; Bewersdorf, J.; Ries, J. Accurate 4Pi Single-Molecule Localization Using an Experimental PSF Model. *Opt. Lett.* **2020**, *45* (13), 3765–3768.
- (62) Kim, J.; Wang, Y.; Zhang, X. Calculation of Vectorial Diffraction in Optical Systems. *J. Opt. Soc. Am. A* **2018**, *35* (4), 526–535.
- (63) Rego, E. H.; Shao, L.; Macklin, J. J.; Winoto, L.; Johansson, G. A.; Kamps-Hughes, N.; Davidson, M. W.; Gustafsson, M. G. L. Nonlinear Structured-Illumination Microscopy with a Photoswitchable Protein Reveals Cellular Structures at 50-nm Resolution. *Proc. Natl. Acad. Sci. U.S.A.* **2012**, *109* (3), E135–E143.
- (64) Zhanghao, K.; Gao, J.; Jin, D.; Zhang, X.; Xi, P. Super-Resolution Fluorescence Polarization Microscopy. *J. Innovative Opt. Health Sci.* **2018**, *11* (01), No. 1730002.
- (65) Rimoli, C. V.; Valades-Cruz, C. A.; Curcio, V.; Mavrakis, M.; Brasselet, S. 4polar-STORM Polarized Super-Resolution Imaging of Actin Filament Organization in Cells. *Nat. Commun.* **2022**, *13* (1), No. 301.
- (66) Wu, T.; Lu, J.; Lew, M. D. Dipole-Spread-Function Engineering for Simultaneously Measuring the 3D Orientations and 3D Positions of Fluorescent Molecules. *Optica* **2022**, *9* (5), 505–511.
- (67) Wang, Z.; Zhao, T.; Hao, H.; Cai, Y.; Feng, K.; Yun, X.; Liang, Y.; Wang, S.; Sun, Y.; Bianco, P. R.; Oh, K.; Lei, M. High-Speed Image Reconstruction for Optically Sectioned, Super-Resolution Structured Illumination Microscopy. *Adv. Photonics* **2022**, *4*, No. 026003.
- (68) Wang, Z.; Zhao, T.; Cai, Y.; Zhang, J.; Hao, H.; Liang, Y.; Wang, S.; Sun, Y.; Chen, T.; Bianco, P. R.; Oh, K.; Lei, M. Rapid, Artifact-Reduced, Image Reconstruction for Super-Resolution Structured Illumination Microscopy. *Innovation* **2023**, *4* (3), No. 100425.

## ■ NOTE ADDED AFTER ASAP PUBLICATION

This paper was originally published ASAP on December 30, 2024. Due to a production error, equations in the Supporting Information were not converted correctly. The revised version reposted on January 15, 2025.